AIAA AVIATION Forum
12-16 June 2023, San Diego, CA and Online
AIAA AVIATION 2023 Forum

10.2514/6.2023-3445

Hypersonic Boundary-Layer Receptivity to Oblique Vorticity Waves

Anand R. Varma*
University of California, Los Angeles, California, 90095, USA

Carleton P. Knisely†
Lawrence Livermore National Laboratory, Livermore, California, 94550, USA

Xiaolin Zhong‡
University of California, Los Angeles, California, 90095, USA

The receptivity of a hypersonic straight-cone boundary layer to freestream vorticity waves was investigated using direct numerical simulation (DNS) and linear stability theory (LST). The setup was a Mach 15 flow over a 0.5-mm-nose-radius straight cone at an altitude of 26 km. The freestream disturbances were oblique planar vorticity waves at various frequencies (400 kHz, 800 kHz, and 1200 kHz) and incident angles. The incident angles ranged from 0° to 29.4° for the 400 kHz case, 0° to 15.7° for the 800 kHz case, and 0° to 10.6° for the 1200 kHz case. In the DNS, the oblique vorticity waves led to a boundary-layer disturbance containing a spectrum of azimuthal wavenumber components. The receptivity coefficients for mode S (the unstable mode) were computed for the 400 kHz case only. For the oblique waves, the receptivity coefficients were found to generally decrease with increasing azimuthal wavenumber. Increasing the incident angle had mixed effects on the receptivity coefficients, depending on the azimuthal wavenumber. While low wavenumber components could be amplified or attenuated, higher wavenumbers beyond a certain value were consistently amplified. For all of the frequencies considered, increasing the incident angle amplified the boundary-layer disturbance at the leeward ray (relative to the freestream wave) and attenuated it at the windward ray in most of the second-mode unstable region, except for a small region near the branch I neutral point.

I. Introduction

Predicting laminar-to-turbulent transition in the boundary layer is critical to the design of hypersonic vehicles, as surface heating and drag can be amplified in a turbulent flow compared to a laminar flow. Transition to turbulence is ultimately caused by external disturbances, such as freestream disturbances or surface roughness. There are several paths by which an external disturbance causes transition, and the specific path taken by a disturbance depends on its initial amplitude. The current study is primarily concerned with transition in a weak external disturbance environment, where transition is not directly caused by external disturbances. Rather, transition occurs through the linear eigenmode growth of boundary-layer modes which are excited by the external disturbance through the so-called receptivity process. This linear eigenmode growth occurs through some instability mechanism. In two-dimensional (2-D) and axisymmetric hypersonic boundary layers, the predominant instability mechanism is Mack's [1] second mode, which is an inviscid instability associated with trapped acoustic waves within the boundary layer. Through this instability, the boundary-layer modes can eventually become large enough to induce nonlinear interactions, after which transition to turbulence begins.

In free-flight scenarios, the presence of turbulence in the atmosphere means that freestream turbulence (FST) must be considered when predicting transition locations. Many researchers (e.g. Ricco and Wu [2], Schrader *et al.*[3], and Ustinov [4]) have used vorticity waves to study receptivity to FST. In fact, vorticity waves can be used to generate complex "synthetic" turbulence fields, using methods like the random Fourier method of Kraichnan [5]. A simple way to study the three-dimensional (3-D) receptivity processes associated with FST would be to consider freestream vorticity waves at nonzero incident angles (oblique waves). For sharp flat plates, the studies of Ma and Zhong [6, 7], Egorov *et al.*[8] and Balakumar *et al.*[9] have shown that incident angle can have play a substantial role in determining

*Ph.D. Student, Mechanical and Aerospace Engineering, varmaar@ucla.edu
†Computational Engineering Division, knisely2@llnl.gov
‡Professor, Mechanical and Aerospace Engineering, xiaolin@seas.ucla.edu

boundary-layer disturbance amplitudes for a variety of freestream waves. For 2-D, "double-sided" geometries, such as wedges and blunted flat plates, the effect of incident angle on receptivity to freestream acoustic waves has been studied by Malik and Balakumar [10] and Balakumar and Kegerise [11]. They found that increasing the incident angle causes boundary-layer disturbance amplitudes to decrease on the windward side (relative to the freestream wave). On the leeward side, variations were less consistent and weaker. For a straight cone geometry, the effect of incident angle on receptivity to slow acoustic waves has been studied by Wan *et al.*[12]. In contrast to the other geometries, here the flowfield was fully 3-D. They found that increasing the incident angle causes boundary-layer disturbance amplitudes to decrease along the windward ray and increase along the leeward ray, with a continuous variation in amplitudes between those rays. In their study, however, the instability mechanism was the first mode, not the second mode. Hence, it is unclear whether the existing results can be extended to vorticity waves and second-mode dominated flows over straight cones.

The objective of the present study is to understand how incident angle affects boundary-layer receptivity to freestream vorticity waves. To that end, we perform an unsteady DNS of boundary-layer receptivity to oblique freestream vorticity waves at various frequencies and incident angles. The paper is organized is follows. We begin with a description of the simulation conditions and the governing equations, after which we describe the numerical methods (DNS and LST) and freestream disturbance model. We present the steady DNS solution and then use LST analysis to characterize the relevant boundary-layer instabilities. Lastly, we present the results of the unsteady DNS, where we impose the vorticity waves onto the freestream, and analyze the resulting boundary-layer disturbance.

II. Simulation Conditions

The flow configuration is a Mach 15 flow over a straight cone with a nose radius of 0.5 mm and half-angle of 5 degrees, at zero angle-of-attack. The freestream conditions correspond to atmospheric conditions at an altitude of 26 km (85 kft) and are shown in Table 1. To better approximate wall temperature distributions found in real flight conditions, we use the approach of Mortensen [13]. In the nose region, wall temperatures are computed by assuming radiative equilibrium at the surface, with a surface emissivity of 0.8. On the cone frustum, the temperature is then exponentially lowered to 1000 K. The resulting wall temperature distribution is shown in Fig. 1. The symbol s denotes the streamwise distance along the surface of the cone, measured from the stagnation point. In addition, we assume a noncatalytic wall in thermal equilibrium (i.e. the translation-rotation temperature is set equal to the vibration temperature).

The computational domain extends to s = 1.8 m and is discretized using 384 points in the wall-normal direction and about 10 points per millimeter in the streamwise direction. In the azimuthal direction, the grid resolution is chosen based on the vertical wavelength (λ_y) of the freestream disturbance. We attempt to maintain a minimum of 6 points per wavelength, which should be sufficient considering that Fourier spectral collocation is used to compute the derivatives in this direction. Due to body divergence, the number of points in the azimuthal direction must be increased moving downstream to maintain a fixed number of points per wavelength. Accordingly, we use 32, 64, and 128 points in the azimuthal direction depending on the streamwise location.

Table 1 Freestream conditions

Parameter	Value	Parameter	Value
M_∞	15	$H_{0,\infty}$	10.34 MJ/kg
ρ_∞	3.405×10^{-2} kg/m^3	p_∞	2188 Pa
T_∞	222.5 K	Re_1	10.5×10^6
Y_{N_2}	0.78	Y_{O_2}	0.22

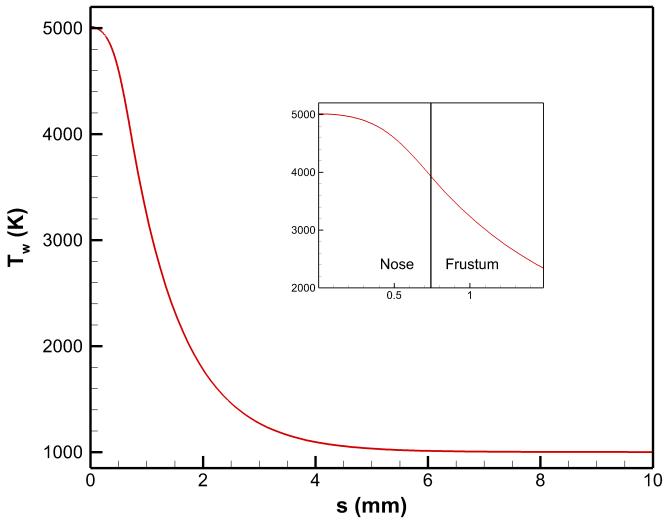

Fig. 1 Wall temperature variation versus streamwise distance

III. Governing Equations and Gas Model

The gas model is formulated for thermochemical nonequilibrium assuming a two-temperature model. The rotational mode is assumed to be fully excited and in equilibrium with the translation mode. Two temperatures are used to represent translation-rotation energy and vibration energy, respectively. The five species model (N_2, O_2, NO, N and O) is used to simulate air chemistry. The governing equations are the Navier-Stokes equations in conservative form, consisting of five species mass conservation equations, three momentum conservation equations, the total energy equation, and the vibration energy equation. The governing equations in vector form are written as

$$\frac{\partial U}{\partial t} + \frac{\partial F_j}{\partial x_j} + \frac{\partial G_j}{\partial x_j} = W \tag{1}$$

where U is the state vector of conserved quantities and W is the source terms defined by

$$U = \begin{bmatrix} \rho_1 \\ \vdots \\ \rho_{ns} \\ \rho u_1 \\ \rho u_2 \\ \rho u_3 \\ \rho e \\ \rho e_v \end{bmatrix}, \quad W = \begin{bmatrix} \omega_1 \\ \vdots \\ \omega_{ns} \\ 0 \\ 0 \\ 0 \\ 0 \\ \sum_{s=1}^{nms} \left(Q_{T-V,s} + \omega_s e_{v,s} \right) \end{bmatrix}.$$

The inviscid and viscous flux vectors, F_j and G_j, respectively, are defined by

$$F_j = \begin{bmatrix} \rho_1 u_j \\ \vdots \\ \rho_{ns} u_j \\ \rho u_1 u_j + p\delta_{1j} \\ \rho u_2 u_j + p\delta_{2j} \\ \rho u_3 u_j + p\delta_{3j} \\ (p + \rho e)\, u_j \\ \rho e_v u_j \end{bmatrix}$$

$$G_j = \begin{bmatrix} \rho_1 v_{1j} \\ \vdots \\ \rho_{ns} v_{nsj} \\ \tau_{1j} \\ \tau_{2j} \\ \tau_{3j} \\ -u_i \tau_{ij} - k_T \frac{\partial T}{\partial x_j} - k_V \frac{\partial T_V}{\partial x_j} + \sum_{s=1}^{nms} \rho_s h_s v_{sj} \\ -k_V \frac{\partial T_V}{\partial x_j} + \sum_{s=1}^{nms} \rho_s e_{v,s} v_{sj} \end{bmatrix}$$

where v_{sj} is the species diffusion velocity, and

$$\tau_{ij} = \mu \left(\frac{\partial u_i}{\partial x_j} + \frac{\partial u_j}{\partial x_i} \right) - \frac{2}{3} \mu \frac{\partial u_k}{\partial x_k} \delta_{ij} \tag{2}$$

is the viscous stress. The total energy per unit volume, ρe, is defined as

$$\rho e = \sum_{s=1}^{ns} \rho_s c_{v,s} T + \rho e_v + \frac{1}{2} \rho \left(u_1^2 + u_2^2 + u_3^2 \right) + \sum_{s=1}^{ns} \rho_s h_s^o \tag{3}$$

where h_s^o is the species heat of formation, $e_{v,s}$ is the species vibration energy, and $c_{v,s}$ is the species translation-rotation specific heat at constant volume, defined as

$$c_{v,s} = \begin{cases} \frac{5}{2} \frac{R}{M_s} & s = 1, 2, \ldots, nms \\ \frac{3}{2} \frac{R}{M_s} & s = nms + 1, \ldots, ns. \end{cases} \tag{4}$$

The vibration energy per unit volume, ρe_v, is defined as

$$\rho e_v = \sum_{s=1}^{nms} \rho_s e_{v,s} = \sum_{s=1}^{nms} \rho_s \frac{R}{M_s} \frac{\theta_{v,s}}{\exp\left(\theta_{v,s}/T_V\right) - 1} \tag{5}$$

where $\theta_{v,s}$ is the characteristic vibrational temperature of each vibrational mode. The characteristic vibration temperatures are taken from Park [14]. To model chemical nonequilibrium, three dissociation reactions and three exchange reactions are used. Each reaction is governed by a forward and backward reaction rate determined from

$$k_f = C_f T_a^{\eta} \exp\left(-\theta_d / T_a\right) \tag{6}$$

$$k_b = k_f / K_{eq} \tag{7}$$

where all forward reaction rates are obtained from Park [14]. The equilibrium coefficient, K_{eq}, is determined by using

$$K_{eq} = A_0 \exp\left(\frac{A_1}{Z} + A_2 + A_3 \ln(Z) + A_4 Z + A_5 Z^2 \right), \tag{8}$$

$$Z = \frac{10000}{T} \tag{9}$$

which is a curve fit to experimental data from Park [14].

The source term in the vibration energy equation representing the exchange of energy between the translation-rotation and vibration energies is calculated using the Landau-Teller formulation:

$$Q_{T-V,s} = \rho_s \frac{e_{v,s}(T) - e_{v,s}(T_V)}{< \tau_s > + \tau_{cs}} \tag{10}$$

where $< \tau_s >$ is the Landau-Teller relaxation time given by Lee [15]. The term τ_{cs} from Park [14] is used to more accurately model the relaxation time in areas of high temperatures occurring just downstream of the bow shock.

The viscosity of each species is computed using a Blottner curve fit shown in Eq. 11, with coefficients from Blottner *et al.*[16]. The mixture viscosity is found using Wilke's [17] mixing rule (Eq. 12-14). The overall heat conductivities for each energy mode are computed in a similar way. The diffusion velocity is calculated using Fick's law (Eq. 15) and a constant Schmidt number of 0.5 (Eq. 16).

$$\mu_s = 0.1 \exp\left[\left(A_s^\mu \ln(T) + B_s^\mu\right)\ln(T) + C_s^\mu\right] \tag{11}$$

$$\mu = \sum_{s=1}^{ns} \frac{X_s \mu_s}{\phi_s} \tag{12}$$

$$X_s = \frac{c_s}{M_s} \tag{13}$$

$$\phi_s = \frac{\sum_{r=1}^{ns} X_r \left[1 + \left(\frac{M_s}{M_r}\right)^{1/4}\right]^2}{\left[8\left(1 + \frac{M_s}{M_r}\right)\right]^{1/2}} \tag{14}$$

$$\rho_s v_{s,j} = -\rho D_s \frac{\partial c_s}{\partial x_j} \tag{15}$$

$$Sc = \frac{\mu}{\rho D} = 0.5 \tag{16}$$

IV. Numerical Methods

A. Direct Numerical Simulation (DNS)

The DNS is performed using the thermochemical nonequilibrium shock-fitting code of Mortensen and Zhong [18–23], which is capable of simulating 5-species or 11-species thermochemical nonequilibrium flow. As is typical of shock-fitting codes, the upper boundary of the computational domain is the shock, which evolves in time. In order to use finite difference stencils, we use a time dependent coordinate transformation of the governing conservation equations written as

$$\begin{cases} \xi = \xi(x,y,z) \\ \eta = \eta(x,y,z,t) \\ \zeta = \zeta(x,y,z) \\ \tau = t \end{cases} \iff \begin{cases} x = x(\xi,\eta,\zeta,\tau) \\ y = y(\xi,\eta,\zeta,\tau) \\ z = z(\xi,\eta,\zeta,\tau) \\ t = \tau \end{cases} \tag{17}$$

where ξ is in the streamwise direction, η is normal to the body, ζ is in the azimuthal direction, $\zeta_t = 0$, and $\xi_t = 0$. The governing equation can then be transformed into computational space as

$$\frac{1}{J}\frac{\partial U}{\partial \tau} + \frac{\partial E'}{\partial \xi} + \frac{\partial F'}{\partial \eta} + \frac{\partial G'}{\partial \zeta} + \frac{\partial E'_v}{\partial \xi} + \frac{\partial F'_v}{\partial \eta} + \frac{\partial G'_v}{\partial \zeta} + U\frac{\partial (1/J)}{\partial \tau} = \frac{W}{J} \tag{18}$$

where J is the Jacobian of the coordinate transformation and

$$E' = \frac{F_1 \xi_x + F_2 \xi_y + F_3 \xi_z}{J} \tag{19}$$

$$F' = \frac{F_1\eta_x + F_2\eta_y + F_3\eta_z}{J} \tag{20}$$

$$G' = \frac{F_1\zeta_x + F_2\zeta_y + F_3\zeta_z}{J} \tag{21}$$

$$E'_v = \frac{G_1\xi_x + G_2\xi_y + G_3\xi_z}{J} \tag{22}$$

$$F'_v = \frac{G_1\eta_x + G_2\eta_y + G_3\eta_z}{J} \tag{23}$$

$$G'_v = \frac{G_1\zeta_x + G_2\zeta_y + G_3\zeta_z}{J}. \tag{24}$$

A seven-point stencil is used to discretize the spatial derivatives

$$\frac{\partial f_i}{\partial x} = \frac{1}{hb_i}\sum_{k=-3}^{3}\alpha_{i+k}f_{i+k} - \frac{\alpha}{6!b_i}h^5\left(\frac{\partial f^6}{\partial^6 x}\right) \tag{25}$$

where

$$\alpha_{i\pm3} = \pm1 + \frac{1}{12}\alpha, \qquad \alpha_{i\pm2} = \mp9 - \frac{1}{2}\alpha$$
$$\alpha_{i\pm1} = \pm45 + \frac{5}{4}\alpha, \qquad \alpha_i = -\frac{5}{3}\alpha$$
$$b_i = 60$$

and where h is the step size, $\alpha < 0$ is a fifth order upwind explicit scheme, and $\alpha = 0$ reduces to a sixth order central scheme. Here the inviscid terms use $\alpha = -6$ which yields a low dissipation fifth-order upwinded difference whereas the viscous terms are discretized using $\alpha = 0$. The derivatives in the transverse direction, if required, are treated with Fourier collocation. Second derivatives are computed by applying the first-order derivative operator twice. Our tests indicate that, because of the absence of numerical dissipation in Fourier collocation, higher azimuthal wavenumber modes can grow unbounded, eventually destroying the solution. Therefore, it is necessary to filter the solution in the azimuthal direction, either through solution filtering, in which the solution is filtered after some fixed number of timesteps or through derivative filtering, in which the Fourier coefficients of the derivatives of the solution are modified. In this paper, the 24th-order exponential derivative filter of Pruett and Chang [24] is used.

The inviscid flux terms are treated using flux splitting,

$$F' = F'^{+} + F'^{-} \tag{26}$$

where

$$F'^{\pm} = \frac{1}{2}(F' \pm \Lambda U) \tag{27}$$

and Λ is a diagonal matrix that ensures F'^{+} and F'^{-} contain only pure positive and negative eigenvalues, respectively. For thermochemical nonequilibrium, the eigenvalues of Λ were derived by Liu and Vinokur [25].

A method-of-lines approach is then used to advance the solution in time. For steady-state computations, the forward Euler method is used to advance the solution. For unsteady computations, the 3rd-order Runge-Kutta method of Shu and Osher [26] is used. The flow conditions immediately behind the shock are calculated from the Rankine-Hugoniot relations. The chemical composition and vibrational energy in the freestream are frozen. The shock is assumed to be infinitely thin, such that there is a constant chemical composition and vibration temperature across the shock. A complete derivation of the thermochemical nonequilibrium shock fitting procedure can be found in the work of Mortensen [23].

B. Linear Stability Theory (LST)

The LST analysis is performed using the thermochemical nonequilibrium LST code of Mortensen and Zhong [20], which was later expanded upon by Knisely and Zhong [27]. The code allows the user to partially relax the parallel mean flow assumption so that the mean wall-normal velocity is no longer assumed to be zero and also implements the freestream shock boundary conditions of Knisely and Zhong [27]. The LST equations are derived from the Navier-Stokes

equations by a perturbation expansion of the form $q = \overline{q} + q'$, where q represents the value of some flow quantity, $\overline{q}$ is the mean flow quantity, and q' is the perturbation quantity. The steady flow terms can then be removed under the assumption that they satisfy the governing equations themselves. The perturbation quantities are assumed to be small such that higher-order terms can be ignored. In addition, it is assumed that the mean flow is parallel, such that the mean flow terms are functions of y only. This is an appropriate assumption since gradients in the wall-normal direction are often negligible compared to gradients in the streamwise direction. The perturbation terms are then assumed to take the form of a normal mode such that $q' = \hat{q}(y) \exp\left[i\left(\alpha x + \beta z - \omega t\right)\right]$, where ω is the circular frequency of the disturbance and α and β are the wave numbers. Note that in this context, x, y, and z are *local* coordinates in the streamwise, wall-normal, and spanwise directions respectively. This study considers the spatial stability problem, where ω and β are real and specified *a priori*. In addition, α is assumed to be complex such that $\alpha = \alpha_r + i\alpha_i$. In spatial stability theory, α_r is the streamwise wave number, and $-\alpha_i$ is the growth rate. A positive value for $-\alpha_i$ corresponds to growth, whereas a negative value of $-\alpha_i$ corresponds to decay. Substituting the normal mode form of the perturbation quantity into the governing equations then yields a set of $ns + 5$ coupled ordinary differential equations of the form

$$\left(\mathbf{A}\frac{d^2}{dy^2} + \mathbf{B}\frac{d}{dy} + \mathbf{C}\right)\vec{\phi} = \vec{0}. \tag{28}$$

where $\vec{\phi} = \left[\hat{\rho}_1, \hat{\rho}_2, \ldots, \hat{\rho}_{ns}, \hat{u}, \hat{v}, \hat{w}, \hat{T}, \hat{T}_V\right]^T$, $\mathbf{A}$, $\mathbf{B}$ and $\mathbf{C}$ are complex square matrices of size $ns + 5$, and ns is the number of species in the gas model. Further details regarding the derivation of these matrices can be found in the work of Knisely [28].

C. Freestream Disturbance Model

For the freestream disturbance, we consider an oblique planar vorticity wave translating through a uniform meanflow in the axial (x) direction at the mean flow velocity u_∞. The model can be written as

$$\begin{bmatrix} u' \\ v' \\ w' \end{bmatrix}_\infty = \begin{bmatrix} \Delta u \\ \Delta v \\ \Delta w \end{bmatrix}_\infty \cos\left[k_x(x - u_\infty t) + k_y y + k_z z + \psi\right] \tag{29}$$

where $(\,)'$ is the perturbation, $\Delta(\,)$ is the amplitude, k_x, k_y, and k_z are the wavenumbers in the axial (x), vertical (y) and spanwise (z) directions, and ψ is the phase angle. In a manner similar to Schrader *et al.* [3], the disturbance is specified with the amplitude function given by

$$\begin{bmatrix} \Delta u \\ \Delta v \\ \Delta w \end{bmatrix}_\infty = \frac{\epsilon u_\infty}{\sqrt{k_x^2 + k_y^2}} \begin{bmatrix} -k_y \\ k_x \\ 0 \end{bmatrix} \tag{30}$$

where ϵ is the scale factor of the velocity perturbation vector. The circular frequency of the disturbance is given by $\omega = k_x u_\infty$. The square-root term in the denominator in Eq. 30 ensures that the amplitude of the wave is independent of k_x and k_y. In this study, we set $k_z = 0$ to reduce the computational workload through symmetry conditions on the y-axis. The incident angle is then $\theta = \tan^{-1}(k_y/k_x)$. The computational setup associated with this disturbance is shown in Fig. 2.

We consider several cases with different values of k_x and k_y, corresponding to different frequencies and incident angles. A description of each case is provided in Table 2. The incident angle is indirectly varied by changing the value of k_y. To save on computational time, cases with the same letter (e.g. case A) are imposed simultaneously to the freestream mean flow in the unsteady DNS. For each wave, the phase angle is chosen randomly from a uniform distribution on the interval $[0,2\pi]$. The scale factor is set to a small value, in this case $\epsilon = 2 \times 10^{-7}$, to ensure linearity. Note that when simultaneously imposing multiple planar waves with different wavenumber vectors in 3-D space, it is difficult to eliminate local peaks where the amplitude exceeds that of each wave. Therefore, ϵ must be small enough so that the maximum amplitude of the overall disturbance (here it would be $\epsilon_{max} = 6 \times 10^{-7}$) still corresponds to a linear disturbance.

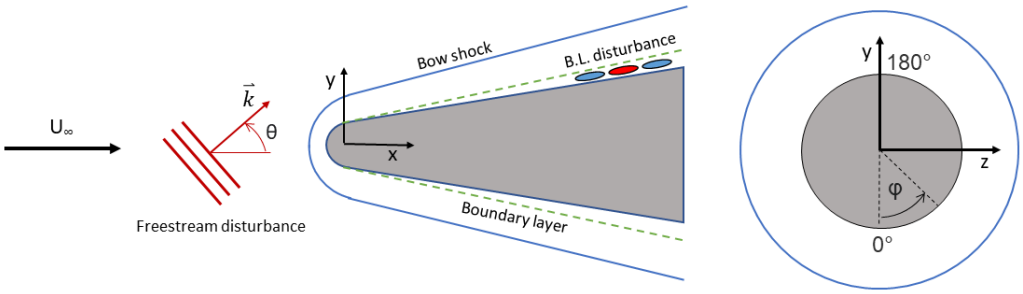

Fig. 2 Schematic of receptivity simulation setup

Table 2 Description of considered cases

Case	k_x (m^{-1})	k_y (m^{-1})	f (kHz)	λ_y (mm)	θ (deg.)
A1	558.5	0	400	-	0
A2	1117	0	800	-	0
A3	1676	0	1200	-	0
B1	558.5	157.1	400	40	15.7
B2	1117	157.1	800	40	8.00
B3	1676	157.1	1200	40	5.35
C1	558.5	314.2	400	20	29.4
C2	1117	314.2	800	20	15.7
C3	1676	314.2	1200	20	10.6

V. Steady DNS Results

Fig. 3a shows the mean flow temperatures in the nose region. The highest translation-rotation temperatures are found at the stagnation line. Thermal nonequilibrium (TNE) effects are fairly strong throughout, as shown by the large differences between T (translation-rotation temperature) and T_v (vibration temperature). Fig. .3b shows the mass fractions of O_2 and O in the nose region. There is a moderate level of chemical nonequilibrium (CNE) effects, as indicated by the mass fraction of O, which reaches about 11% at the stagnation point, primarily through the dissociation of O_2. While other reactions are present in the flowfield (e.g. dissociation of N_2 into N), the lower levels of O_2 toward the wall mean that O_2 dissociation is the dominant reaction in the flowfield. This is due to the fact that O_2 dissociation begins to occur at lower temperatures than N_2 dissociation.

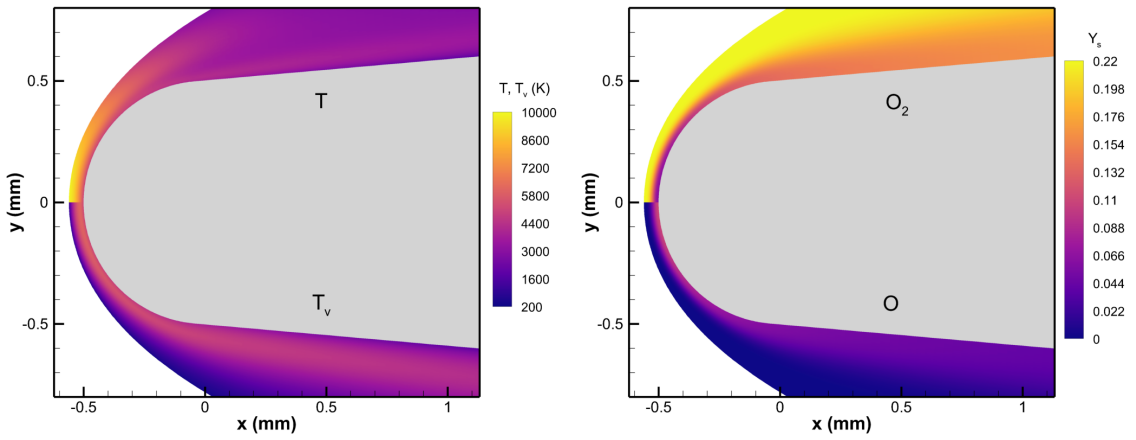

(a) (b)

Fig. 3 Steady DNS contours of various quantities in the nose region. (a) Translation-rotation and vibration temperature. (b) Mass fraction of O_2 and O.

Fig. 4 shows the typical wall-normal mean flow profiles of streamwise velocity, temperature and the mass fraction of O on the cone frustum, in this case located at $s = 0.1$ m. The large discrepancies in the profiles of T and T_v indicate that TNE effects are still fairly strong. In contrast, the minuscule amounts of O suggest that CNE effects are weak. This means that while TNE effects could have a significant impact on boundary-layer stability, CNE effects are likely negligible. Regarding TNE, Knisely and Zhong [29] found that for a Mach 5 flow, if $T < T_v$ (as is the case here), TNE effects can have a destabilizing effect on the second-mode instability, leading to higher growth rates, extended unstable regions and higher N-factor envelopes when compared to a frozen flow. Furthermore, since the receptivity process begins at the leading edge, where both TNE and CNE effects are much stronger, both of those effects could be significant in that regard.

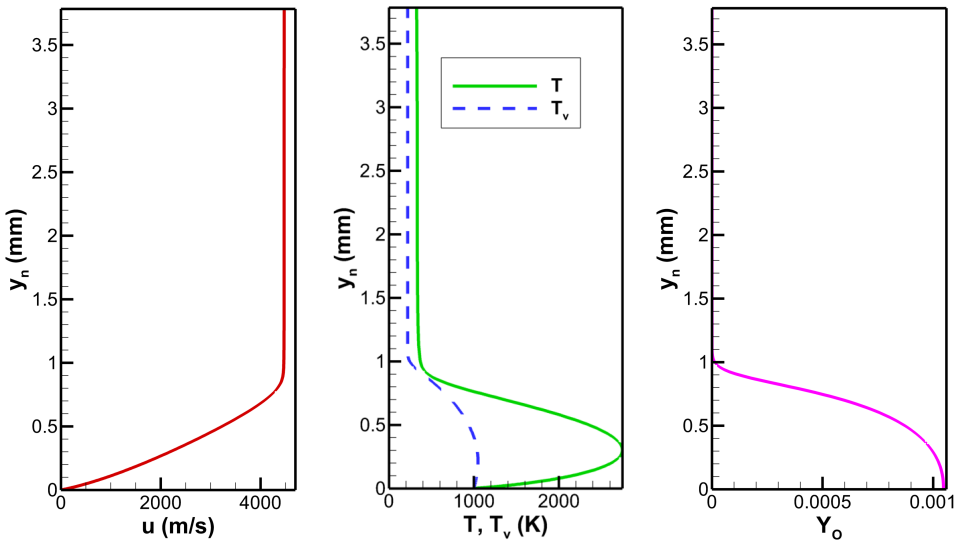

Fig. 4 Wall-normal profiles of various mean flow quantities at s = 0.1 m, obtained from steady DNS. (a) Wall-tangent velocity. (b) Translation-rotation and vibration temperatures. (c) Mass fraction of O.

VI. LST Results

To identify the unstable mode and its characteristics, we perform linear stability theory (LST) analysis on the steady DNS mean flow. Fig. 5 shows the streamwise behavior of the relevant boundary-layer modes in terms of streamwise phase speed and growth rate at f = 400 kHz. Note that k_c is the azimuthal wavenumber, which is the number of wavelengths around the circumference of the cone. For axisymmetric waves, $k_c = 0$. Since the domain is periodic in the azimuthal direction, only integer values of k_c are admissible. The two relevant boundary-layer modes are mode S and mode F_1. Mode S begins in the slow acoustic spectrum near the leading edge, and increases in phase speed downstream. Conversely, mode F_1 begins in the fast acoustic spectrum near the leading edge, but decreases in phase speed downstream. Mode F_1 eventually coalesces with the entropy/vorticity spectrum downstream, at which point a new mode emerges [30]. However, to be consistent with the literature, we treat mode F_1 as if it were a single mode. Even further downstream, mode S and F_1 become coupled, as indicated by their "mirrored" growth rate plots. This destabilization of mode S is consistent with the second-mode instability.

A more complete view of the behavior of the mode S can be found from a stability map, which is shown in Fig. 6 for various values of k_c. The contoured regions indicate the range of frequencies and streamwise locations at which mode S is unstable. The point at which mode S initially becomes unstable is called the branch I neutral point, whereas the point at which it becomes stable again is called the branch II neutral point. Evidently there is also a third-mode instability, associated with the coupling of mode S with mode F_2 (a higher mode similar to mode F_1), as well as a first-mode instability, which is the compressible analog of the Tollmien-Schlichting wave. The third mode and first mode instabilities occur at higher and lower frequency ranges, respectively, when compared to the second-mode instability. However, these additional instabilities are not expected to be relevant to transition due to their relatively small growth rates. The stability map also shows that increasing k_c leads to a smaller unstable second mode frequency range and lower peak growth rates, although this effect is less noticeable moving downstream.

It is possible to predict transition locations using the so-called e^N method, in which one of the key assumptions is that transition occurs once an unstable mode at a given frequency and azimuthal wavenumber reaches a certain amplitude ratio, or N-factor, defined as

$$N(s, f, k_c) = \ln\left(\frac{A(s, f, k_c)}{A_0(f, k_c)}\right) = \int_{s_0(f,k_c)}^{s} -\alpha_i(s, f, k_c)ds \tag{31}$$

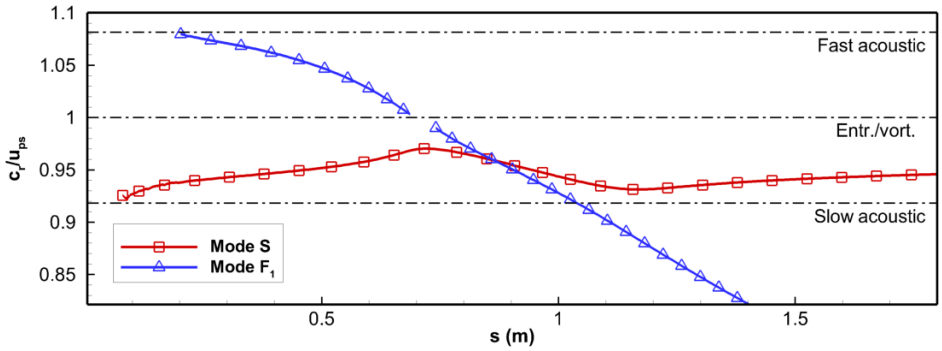

(a)

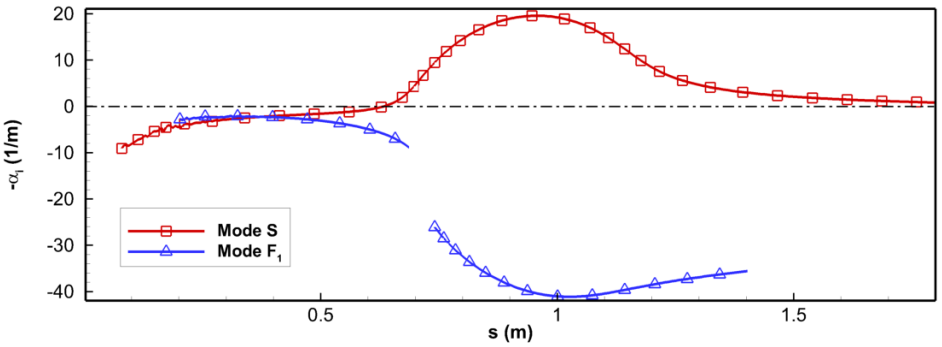

(b)

Fig. 5 Streamwise behavior of relevant axisymmetric (k_c = 0) discrete modes at f = 400 kHz, obtained from LST. (a) Streamwise phase speed. (b) Growth rate. The horizontal lines in the phase speed plot denote the phase speeds of the 2-D continuous spectra. Discrete mode phase speeds are normalized using the post-shock streamwise velocity u_{ps} = 4473 m/s. Continuous spectra phase speeds are computed using the post-shock Mach number M_{ps} = 12.26.

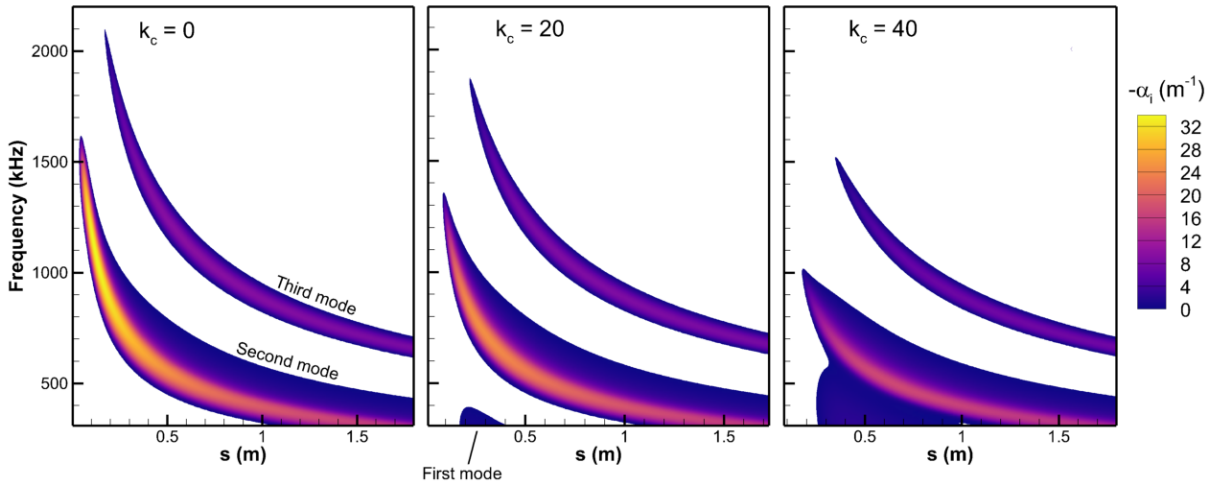

Fig. 6 LST mode S stability map for selected values of k_c. Only unstable regions are contoured.

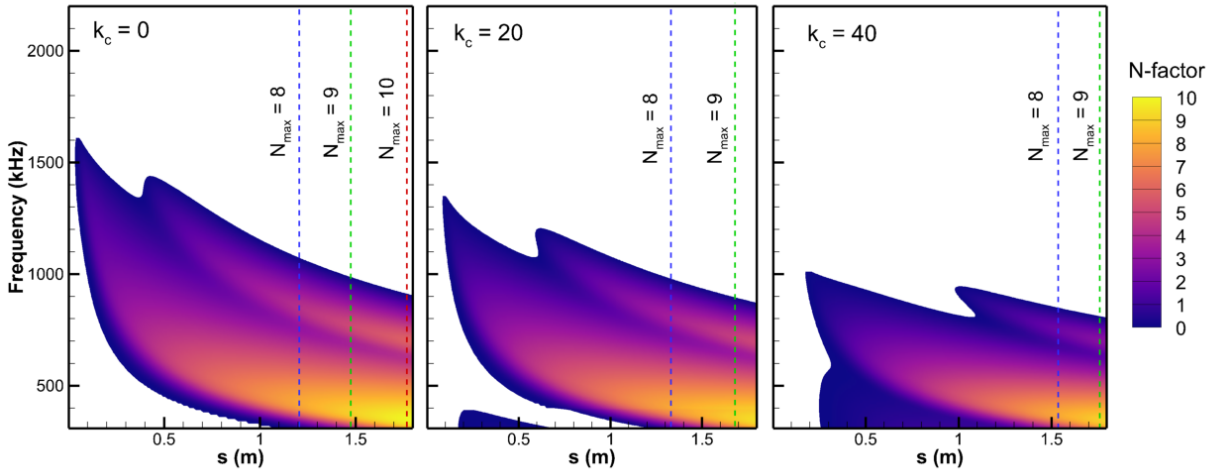

Fig. 7 LST mode S N-factor map for selected values of k_c. N-factors associated with only third-mode amplification are not shown. For each frequency, N-factors are computed relative to the first point at which mode S becomes unstable.

where A is the disturbance amplitude at some streamwise location downstream of the branch I neutral point, A_0 is the amplitude at the branch I neutral point (the initial amplitude), and s_0 is the location of the branch I neutral point. In free-flight, transition N-factors are usually around 10 or more. Fig. 7 shows the N-factor map for mode S at various azimuthal wavenumbers. The dashed vertical lines indicate the location at which the highest N-factor out of all frequencies (the N-factor envelope) reaches a given value. For instance, at $k_c = 0$, the N-factor envelope reaches a value of 10 around $s = 1.76$ m. This "level" is indicated by the red dashed line. Here, increasing k_c has a stabilizing effect, since the point at which the N-factor envelope reaches each level moves downstream. This is not much of a surprise, as it is well-known that the axisymmetric second-mode disturbance is most unstable for straight cone geometries at zero angle-of-attack.

VII. Unsteady DNS Results

In this section, we present the results of the DNS receptivity simulations involving the freestream vorticity disturbances described in Table 2. Recall from Section IV that vorticity waves with the same vertical wavenumber (k_y), but different frequencies are imposed simultaneously. To extract the flowfield at each frequency, we apply a 1-D FFT in time to the unsteady DNS data. To extract the flowfield at each frequency *and* azimuthal wavenumber, we apply a 2-D FFT in time and in the azimuthal direction. In all of the figures shown, the disturbance quantities (density or pressure fluctuations) are nondimensionalized by their freestream mean values (ρ_∞ or p_∞), and then normalized by the amplitude of the freestream disturbance (ϵ).

A. General Description of Flowfield

To begin, we consider some of the DNS results from the $f = 400$ kHz, $\theta = 29.4°$ case to demonstrate the typical characteristics of the unsteady flowfield. Fig. 8 shows the instantaneous density fluctuation field in the upstream region of the cone (up to $s = 50$ mm). Starting from the nose and moving downstream, the freestream vorticity wave interacts with the shock and then transmits/generates disturbances behind the shock. These post-shock disturbances then enter the boundary layer. The boundary-layer disturbance then grows moving downstream, eventually overtaking the freestream disturbance in amplitude. This upstream growth is not due to second-mode amplification, which occurs further downstream. Instead, it is related to the leading-edge receptivity process. The disturbance is concentrated primarily on the leeward ($\varphi = 180°$) and windward rays ($\varphi = 0°$), and is attenuated significantly along the $\varphi = 90°$ ray. Here, the terms leeward and windward refer to the rays of the cone facing away and towards the freestream disturbance respectively. Towards the end of this upstream region, the boundary-layer disturbance is noticeably stronger on the

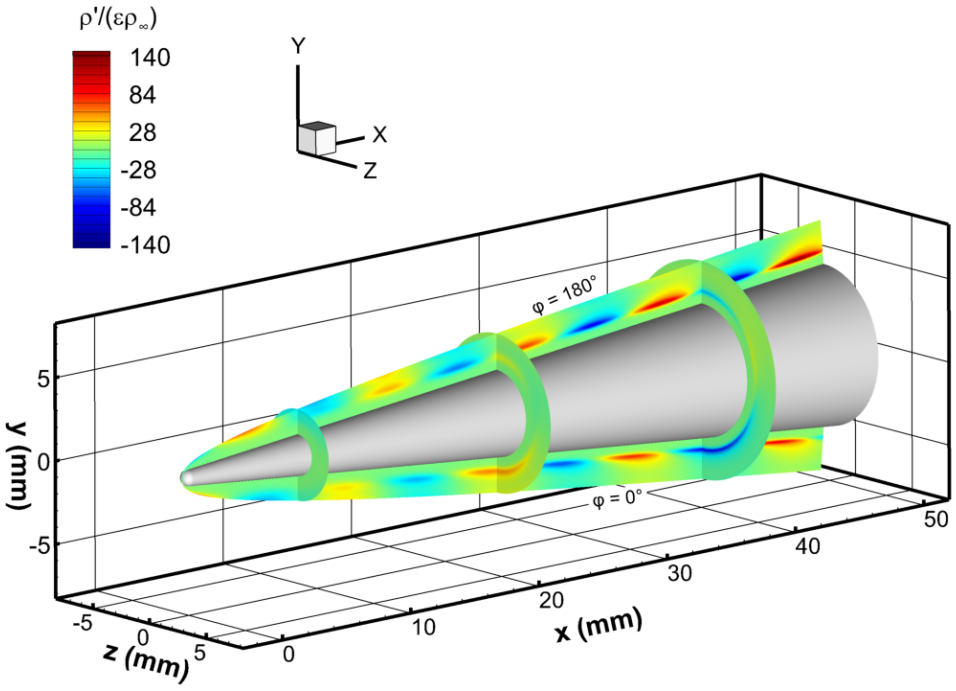

Fig. 8 Instantaneous density fluctuation field in upstream region. (f = 400 kHz, θ = 29.4°)

leeward ray compared to the windward ray. Fig. 9 shows the instantaneous density fluctuation field much further downstream (around s = 1 m), where mode S (the unstable mode) has become unstable through the second-mode instability. The fluctuations are typical of the second-mode instability, with visible perturbations at the wall and the critical layer (the wall-normal distance at which the phase speed of the unstable mode is equal to the mean streamwise velocity), which is close to the boundary-layer edge. The amplitude on the leeward ray is again seen to be stronger than on the windward ray, but this variation is much more prominent here.

Fig. 11 shows a 2-D map of the wall-pressure fluctuation amplitude in s-φ space. The amplification at the end of the domain corresponds to the second-mode instability. It is again apparent that the disturbance is stronger on the leeward ray ($\varphi = 180°$) than the windward ray ($\varphi = 0°$). However, the minimum amplitude occurs close to the $\varphi = 90°$ ray. Fig. 10 shows a 2-D map of the wall-pressure fluctuation amplitude in s-k_c space. This map is obtained by applying a 2-D FFT (in time and in the azimuthal direction) to the wall-pressure fluctuation at each streamwise location. The region upstream of the branch I neutral point is marked by areas of local amplification and decay associated with the leading-edge receptivity process, whereby the internal modes (mode S, mode F_1, etc.) undergo forcing from the external waves originating from the interaction of the freestream vorticity waves with the shock. There is also constructive/destructive interference between modes here. The specific receptivity mechanism will be considered in a future study. At any given streamwise location the amplitude generally decreases with increasing k_c. Moving downstream, the azimuthal spectrum becomes broader. This spectral broadening was also noted by Balakumar [31] in his study of receptivity to acoustic freestream waves for an axisymmetric cone. In the second-mode amplification region, there is an abrupt dip in amplitude at $k_c = 4$, causing a dark horizontal line to appear in the contours. It is still unclear as to what causes this behavior.

B. Effect of Incident Angle on Receptivity Coefficients

We now consider the effect of incident angle on the resulting boundary-layer disturbance. Fig. 12 shows a comparison of the azimuthal spectrum of the wall-pressure fluctuation at s = 1.1 m for the cases at f = 400 kHz. As will be shown later, the disturbance at this location is expected to be dominated by mode S (due to second-mode amplification). Note that the zero incident angle disturbance excites only a single k_c component, specifically $k_c = 1$, which is represented as a single point. In both of the nonzero incident angle cases, it can be seen that the amplitudes generally decrease with increasing k_c. If we increase the incident angle, the low k_c components are affected inconsistently. That is, while the amplitudes increase for k_c between 0 and 2, they also decrease for k_c between 3 and 7. On the other hand, increasing the

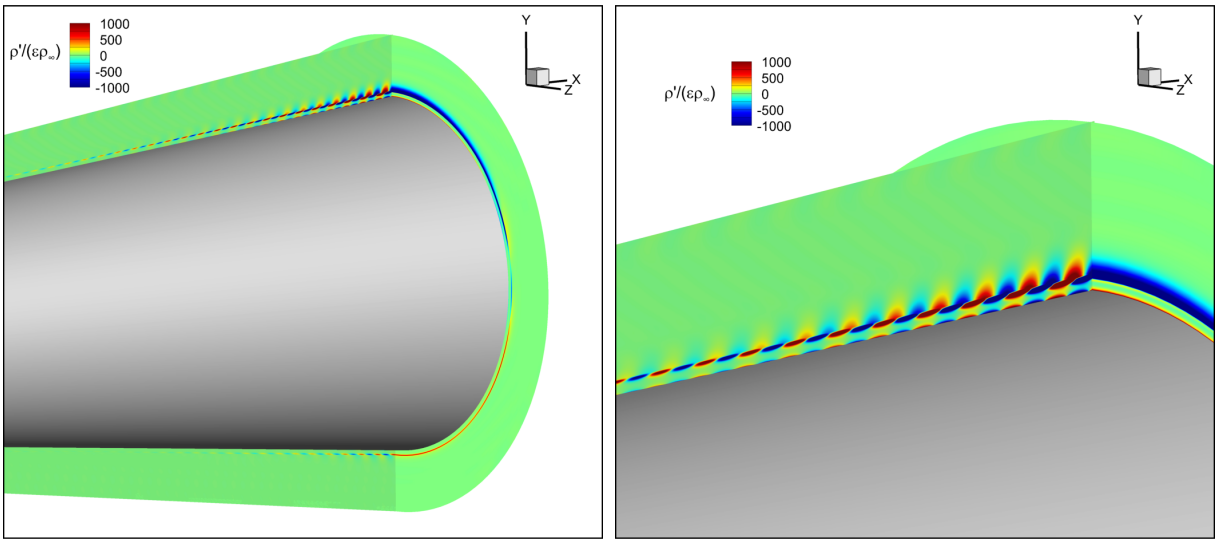

Fig. 9 Instantaneous density fluctuation contours downstream, near s = 1 m. (a) zoomed-out, (b) zoomed-in. Contours are clipped to better show disturbance structure. (f = 400 kHz, θ = 29.4°)

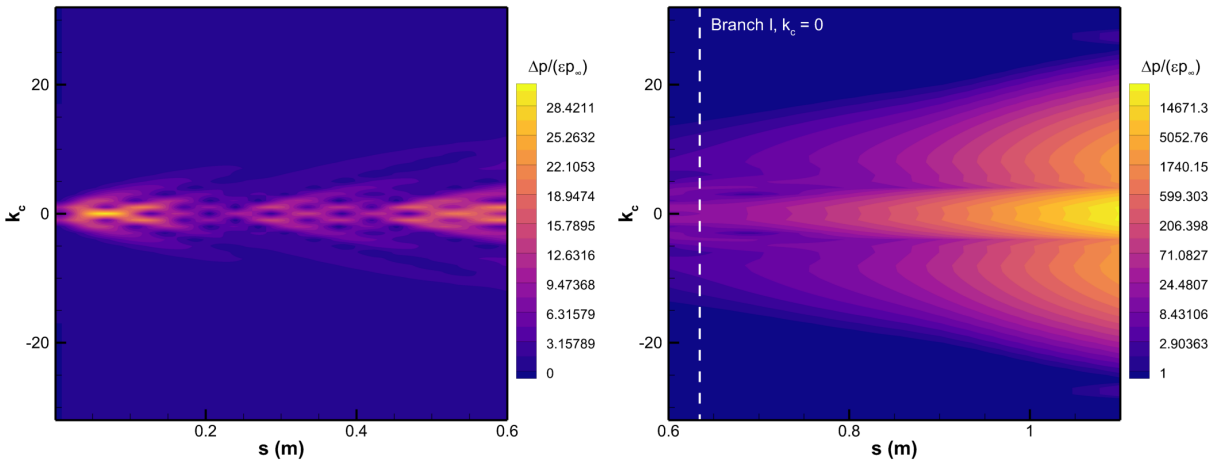

Fig. 10 Unsteady DNS contours of Fourier-transformed wall-pressure fluctuation amplitude in s-k_c space (a) upstream and (b) downstream. An exponential distribution of contour levels is used in (b) to better illustrate exponential growth via the second-mode instability. Note that only integer values of k_c are actually admissible. (f = 400 kHz, θ = 29.4°)

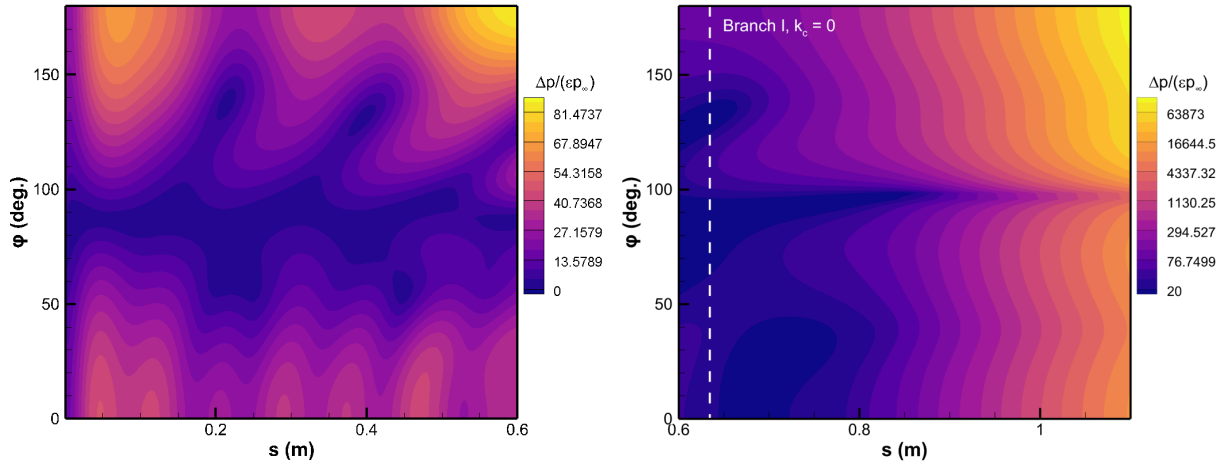

Fig. 11 Unsteady DNS contours of Fourier-transformed wall-pressure fluctuation amplitude in s-φ space (a) upstream and (b) downstream. An exponential distribution of contour levels is used in (b) to better illustrate exponential growth via the second-mode instability. (f = 400 kHz, θ = 29.4°)

incident angle causes the highest k_c components (in this case $k_c \geq 8$) to consistently amplify. Despite this increase, the higher k_c components are still very weak compared to their low k_c counterparts, bringing into question their relevance to transition.

Next we consider the receptivity coefficients, which are the amplitudes of the unstable mode at its branch I neutral point. In the DNS, the boundary-layer disturbance contains many competing modes. In order to extract receptivity coefficients from the DNS, it is necessary to isolate the amplitude of the unstable mode from the overall disturbance. There are a couple of methods available to achieve this, the most rigorous of which is multimodal decomposition, which Gaydos and Tumin [32] and Miselis *et al.*[33] have used to great effect. However, the multimodal decomposition method has not yet been extended to real-gas flows. For this study, we use a more approximate method from Ma and Zhong [34], involving LST-derived N-factors. This method relies on the fact that in the DNS, the unstable mode will eventually dominate the overall disturbance after amplification. Therefore it is possible to "backtrack" the initial amplitude of the unstable mode by (1) sampling the DNS disturbance amplitude at a location where the unstable mode is dominant and (2) dividing that amplitude by the LST N-factor at that location. Hence the receptivity coefficient, denoted by C_R, can be computed as

$$C_R(f, k_c) = A_0(f, k_c) = \frac{A(s, f, k_c)}{e^{N(s,f,k_c)}} \tag{32}$$

where A is some measure of the DNS disturbance amplitude and N is the N-factor obtained from LST, both of which are evaluated at the sampling location s for a given frequency and azimuthal wavenumber.

Based on the requirement that the disturbance be dominated by mode S (the unstable mode), we find a sampling point as close as possible to the branch II neutral point, where LST predicts mode S to be at its maximum amplitude. At f = 400 kHz, the branch II neutral point is located downstream of s = 1.8 m. However, the unsteady DNS was only performed up to s = 1.1 m. Hence, s = 1.1 m was chosen to be the sampling location. It can be confirmed that mode S is dominant at this location by comparing the phase speed and growth rate with the LST results. Such a comparison is shown in Fig. 13. Here, the DNS phase speed and growth rate were obtained from an FFT of the wall-pressure fluctuation. Looking at the phase speed, there is good agreement between the DNS and LST starting from $s \approx 0.8$ m, and the relative difference in values at s = 1.1 m is only about 0.7%. The growth rates do not agree that well, but the DNS growth rate does appear to oscillate about the LST growth rate. The discrepancy in growth rate is most likely due to nonparallel effects, which are neglected in LST. That is, in a growing boundary layer, the growth rate of the unstable mode will vary according to the disturbance quantity (pressure, density, etc.) and the wall-normal distance. In the LST framework, all quantities and wall-normal distances are given the same growth rate. This means that there could be noticeable discrepancies in the growth rate between the DNS and LST, even if the unstable mode is dominant. We also

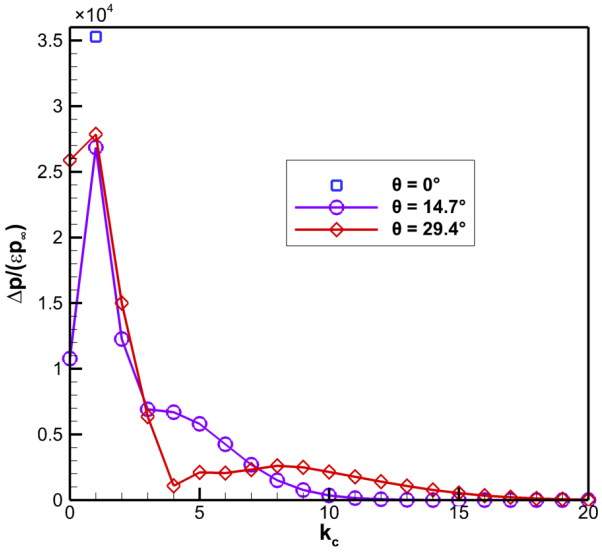

Fig. 12 Comparison of Fourier-transformed wall-pressure fluctuation amplitudes vs. azimuthal wavenumber at s = 1.1 m. Only positive values of k_c are shown due to symmetry. (f = 400 kHz)

computed growth rates using the density perturbation close to the critical layer (where the fluctuation amplitudes are highest), and found that the DNS growth rate still does not match particularly well with the LST results. Hence, for simplicity, we use the wall-pressure fluctuation amplitude, specifically the normalized version given by $\Delta p/(\epsilon p_\infty)$, to compute the receptivity coefficients. We caution that due to the issues mentioned above, there is a fair bit of uncertainty regarding the exact values of these coefficients. Nevertheless, the overall trends (like the effect of incident angle) should be the same.

Fig. 14 shows the azimuthal receptivity coefficient spectra for mode S for the cases at f = 400 kHz. Again these coefficients were computed using s = 1.1 m as the sampling location. Here the receptivity coefficient for each k_c is normalized by the same value, which in this case is the amplitude of the freestream disturbance (denoted by ϵ). This is done because there is no fixed azimuthal spectrum by which the receptivity coefficients can be normalized. As shown by Varma *et al.*[35], the azimuthal spectrum of an oblique vorticity wave varies according to the distance from the cone axis (the radial coordinate). This is in contrast to the study of He and Zhong [36], where receptivity coefficients were normalized on a spectral basis, i.e. the receptivity coefficient spectrum was divided by the corresponding spectrum in the freestream disturbance, rather than a fixed value. The receptivity coefficient spectra look almost exactly the same as the overall disturbance spectra at s = 1.1 m (see Fig. 12) aside from the lower overall amplitudes, so the discussion is also the same. When we increase the incident angle, the low k_c components are again affected inconsistently, whereas for high k_c (specifically $k_c \geq 8$) components, the amplitude increases consistently.

C. Effect of Incident Angle on Overall Disturbance

Fig. 15 shows the azimuthal variation of the wall-pressure fluctuation amplitude at s = 1.1 m for the cases at f = 400 kHz. Similar variations are found in most of the second-mode unstable region except for a small region near the branch I neutral point. At $\theta = 0°$, the amplitudes are the same on the windward and leeward rays. When the incident angle is increased, the amplitude increases on the leeward ray and decreases on the windward ray. This shift of amplitudes at the windward and leeward rays is similar to the results of Wan *et al.*[12], even though they considered slow acoustic waves. The only difference is that in our study, the minimum amplitude occurs at or near the $\varphi = 90°$ ray, whereas in their study, the minimum amplitude is at the windward ray. The present results also show some similarities to the results of Malik and Balakumar [10] and Balakumar and Kegerise [11], who considered acoustic waves and 2-D geometries, i.e. wedges and blunted flat plates. Their studies also found that as the incident angle increases, the disturbance amplitude decreases on the windward side. However, the disturbance amplitude varied less consistently and more weakly on the leeward side. Note that because their geometry was 2-D, there was no continuous variation of amplitudes between the leeward and

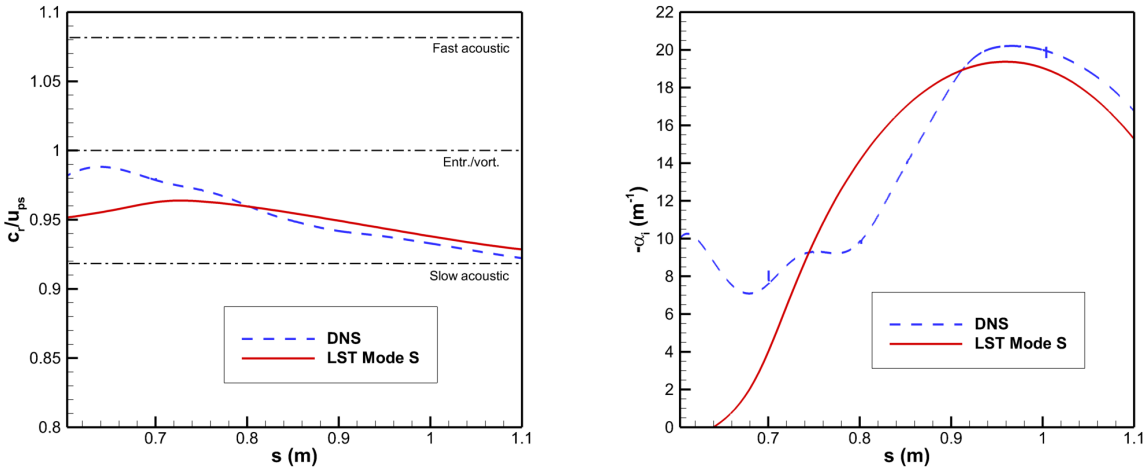

(a) (b)

Fig. 13 Comparison of (a) streamwise phase speed and (b) growth rate between DNS (using wall-pressure fluctuations) and LST at k_c = 10. (f = 400 kHz, θ = 29.5°)

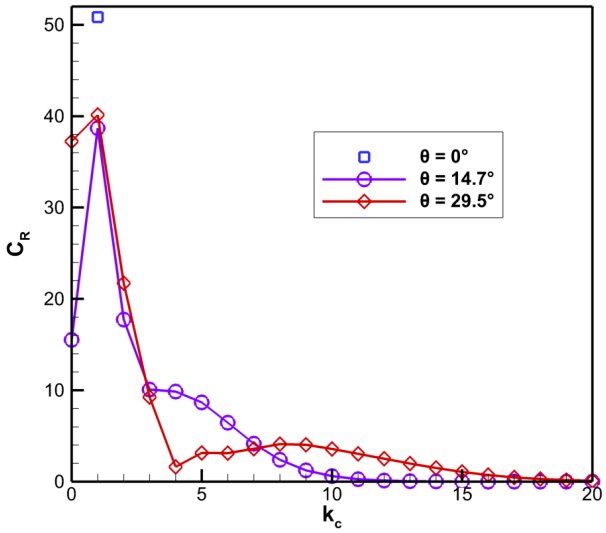

Fig. 14 Comparison of receptivity coefficient spectra using s = 1.1 m as the sampling location. Only positive values of k_c are shown due to symmetry. (f = 400 kHz)

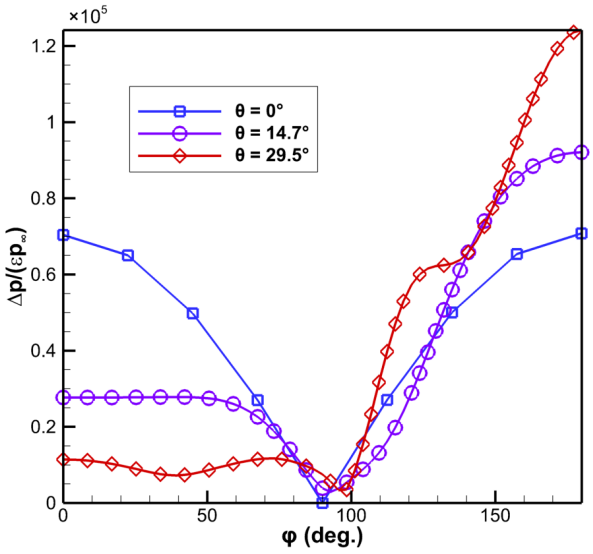

Fig. 15 Comparison of Fourier-transformed wall-pressure fluctuation amplitudes vs. azimuthal angle at s = 1.1 m. (f = 400 kHz)

windward sides.

It is interesting to note that although the two nonzero-incident-angle cases have smaller peak amplitudes in their azimuthal spectra compared to the $\theta = 0°$ case (see Fig. 12), those cases have higher amplitudes along the leeward ray. This suggests that there is constructive interference between different azimuthal components. Understanding this effect requires further study. In particular, phase angle data for mode S could be useful in this regard. The changes in amplitude along the leeward and windward rays when increasing the incident angle is particularly interesting in terms of transition prediction. The experiments of Marineau *et al.*[37] have shown that transition locations can be correlated with the amplitude (specifically the root-mean-square, RMS) of the local wall pressure fluctuation, normalized by the mean pressure at the boundary-layer edge. While the disturbance amplitudes in the present study are far too low to cause transition, the effect of incident angle on potential transition locations can be still be understood from the trends seen here. In particular, the results suggest that if the incident angle is increased, transition locations could move upstream on the leeward ray (due to higher amplitudes) and downstream on the windward ray (due to lower amplitudes).

D. Frequency Effects

We now consider the unsteady DNS results for the two higher frequencies (f = 800 kHz and f = 1200 kHz). Note that at these frequencies, the combination of weaker instabilities (low N-factors) and upstream-shifted unstable regions makes receptivity coefficients difficult to obtain and potentially misleading. As such, we did not compute receptivity coefficients for these cases. Also note that the incident angles span a smaller range of values. This is because for a high frequency wave (high k_x), we must increase k_y to a larger value to get the same incident angle as a low frequency wave. However, if k_y is large, the vertical wavelength λ_y will be very small, which means that a much larger number of points must be used in the azimuthal direction, increasing the computational workload substantially. To use the same azimuthal resolution as the f = 400 kHz cases, we are limited to a smaller range of incident angles.

A comparison of the azimuthal spectra of the wall-pressure fluctuations at these frequencies are shown in Fig. 16. The spectra are evaluated at streamwise locations where the wall-pressure fluctuations attain their highest amplitudes within the second-mode unstable region. The azimuthal spectra (and variations) at most other locations within the unstable region look similar, except for a small region near the branch I neutral point. Compared to the f = 400 kHz cases, the azimuthal spectra are qualitatively similar. As k_c increases, the amplitudes generally decrease. When the incident angle is increased, there does not appear to be a clear pattern of variations in the spectra at low k_c, with some components being amplified while others are attenuated. In contrast, the highest k_c components ($k_c \geq 3$ for f = 800 kHz and $k_c \geq 2$ for f = 1200 kHz) are consistently amplified. But again, these components are still weak compared to

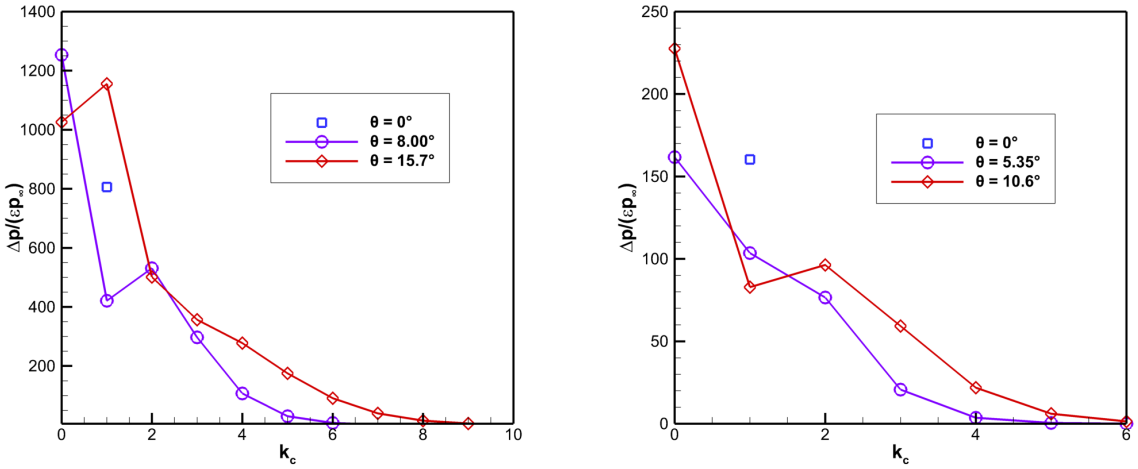

(a) (b)

Fig. 16 Comparison of Fourier-transformed wall-pressure fluctuation amplitude spectra for (a) f = 800 kHz at s = 0.31 m. and (b) f = 1200 kHz at s = 0.134 m. Only positive values of k_c are shown due to symmetry.

the low k_c components. The azimuthal variation of the wall-pressure fluctuations at the same locations are shown in Fig. 17. Like the f = 400 kHz cases, increasing the incident angle leads to an increase in amplitude on the leeward ray and a decrease in amplitude on the windward ray. There are a few notable differences between these results and those at f = 400 kHz. Perhaps the most obvious is that the azimuthal spectrum falls off with increasing k_c much more quickly, such that a much smaller range of k_c are actually relevant. The other is that the overall amplitudes are much smaller. This is likely due to the much lower N-factors at these frequencies. Lastly, the $\theta = 0^\circ$ wave no longer produces the highest amplitude within the azimuthal spectrum.

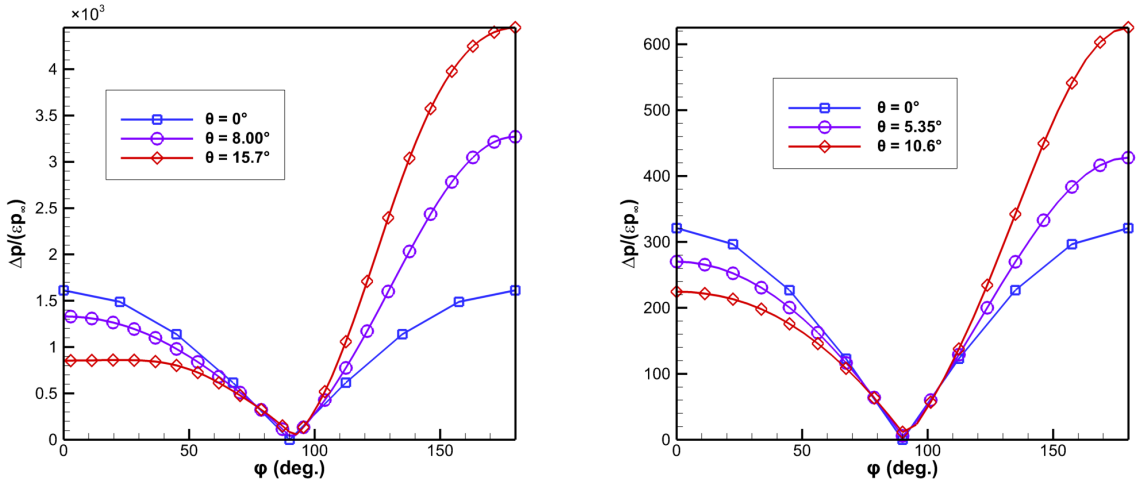

(a) (b)

Fig. 17 Comparison of Fourier-transformed wall-pressure fluctuation amplitudes vs. azimuthal angle for (a) f = 800 kHz at s = 0.31 m. and (b) f = 1200 kHz at s = 0.134 m.

VIII. Summary and Conclusion

We investigated the receptivity of a hypersonic boundary-layer over a Mach 15 straight cone to freestream oblique vorticity waves at various frequencies and incident angles using a combination of DNS and LST. LST results showed that the second-mode instability was dominant, with mode S being the unstable mode. Oblique mode S waves were overall more stable since their N-factor envelopes reached certain values further downstream compared to the axisymmetric wave. Unsteady DNS results showed that the oblique freestream vorticity waves led to a boundary-layer disturbance containing a spectrum of azimuthal wavenumber components. Receptivity coefficient spectra were computed for the low frequency case (f = 400 kHz). For the oblique freestream waves, the receptivity coefficients generally decreased with increasing azimuthal wavenumber. Increasing the incident angle had mixed effects on receptivity coefficients, depending on the azimuthal wavenumber. Although low wavenumber components could be amplified or attenuated, the higher wavenumber components beyond a certain value were consistently amplified. Again, note that we did not obtain receptivity coefficients for the two higher frequency (f = 800 kHz and f = 1200 kHz) cases, which means the results at those frequencies may be different. Unlike the receptivity coefficient spectra, the azimuthal variation of the boundary-layer disturbance gave a more straightforward result. For all of the frequencies considered, increasing the incident angle within their respective ranges amplified the boundary-layer disturbance at the leeward ray and attenuated it at the windward ray in most of the second-mode unstable region, except for a small region near the branch I neutral point.

In order to make a connection between the receptivity coefficients and the amplitudes along the leeward/windward rays, it will be necessary to analyze the phase angles of mode S. This will be accomplished in a future study. Also note that there are two main limitations in this study. Because we performed these simulations for a limited range of incident angles, it still remains to be seen what happens when incidence angles are increased even further. This is especially true for the two higher frequency cases, which were more limited in the range of incident angles considered. In addition, we considered a very specific type of vorticity wave, in which the resulting velocity field is symmetric about the xy-plane. However, there can also exist vorticity waves with the same incident angle, but different velocity components, yielding a velocity field with no symmetry plane. In these cases, the conclusions could be different, so they require additional study.

IX. Acknowledgments

This work was performed under the auspices of the U.S. Department of Energy by Lawrence Livermore National Laboratory (LLNL) under contract #DE-AC52-07NA27344. This work was also supported by LLNL under subcontract

#B642550. Computational resources were provided by the Livermore Computing Center under LLNL subcontract #B642550. The views and conclusions contained herein are those of the authors and should not be interpreted as necessarily representing the official policies or endorsements, either expressed or implied, of the U.S. Department of Energy or the U.S. Government.

References

[1] Mack, L. M., "Boundary Layer Linear Stability Theory," Tech. rep., AGARD report No. 709, 1984.

[2] Ricco, P., and Wu, X., "Effect of free-stream turbulence on a compressible laminar boundary layer," *Fluid Mechanics and its Applications*, Vol. 78, 2006.

[3] Schrader, L.-U., Brandt, L., Mavriplis, C., and Henningson, D., "Receptivity to free-stream vorticity of flow past a flat plate with elliptic leading edge," *Journal of Fluid Mechanics*, Vol. 653, 2010, pp. 245–371.

[4] Ustinov, M. V., "Boundary layer receptivity to the nonlinearly developing freestream turbulence," *Fluid Dynamics*, Vol. 48, 2013, pp. 621–635.

[5] Kraichnan, R., "Diffusion by a random velocity field," *Physics of Fluids*, Vol. 13, No. 1, 1970, pp. 22–31.

[6] Ma, Y., and Zhong, X., "Receptivity of a supersonic boundary layer over a flat plate. Part 2. Receptivity to free-stream sound," *Journal of Fluid Mechanics*, Vol. 488, 2003, pp. 31–78.

[7] Ma, Y., and Zhong, X., "Receptivity of a supersonic boundary layer over a flat plate. Part 3. Effects of different types of free-stream disturbances," *Journal of Fluid Mechanics*, Vol. 488, 2003, pp. 31–78.

[8] Egorov, I. V., Fedorov, A. V., and Soudakov, V. G., "Direct numerical simulation of supersonic boundary-layer receptivity to acoustic disturbances ," *AIAA 2005-97*, 2005.

[9] Balakumar, P., King, R., Chou, A., Owens, L., and Kegerise, M., "Receptivity and Forced Response to Acoustic Disturbances in High-Speed Boundary Layers," *AIAA 2016-3193*, 2016.

[10] Malik, M., and Balakumar, P., "Acoustic receptivity of Mach 4.5 boundary layer with leading-edge bluntness," *Theoretical Computational Fluid Dynamics*, Vol. 21, 2006, pp. 323–342.

[11] Balakumar, P., and Kegerise, M., "Receptivity of Hypersonic Boundary Layers to Acoustic and Vortical Disturbances," *AIAA 2015-2473*, 2011.

[12] Wan, B., Chen, J., Yuan, X., Hu, W., and Tu, G., "Three-Dimensional Receptivity of a Blunt-Cone Boundary Layer to Incident Slow Acoustic Waves," *AIAA Journal*, Vol. 60, No. 8, 2022, p. 4523–4531.

[13] Mortensen, C. H., "Toward an understanding of supersonic modes in boundary-layer transition for hypersonic flow over blunt cones," *Journal of Fluid Mechanics*, Vol. 846, 2018, pp. 789–814.

[14] Park, C., *Nonequilibrium Hypersonic Aerothermodynamics*, John Wiley & Sons Inc., New York, 1990.

[15] Lee, J., "Basic Governing Equations for the Flight Regimes of Aeroassisted Orbital Transfer Vehicles," *Thermal Design of Aeroassisted Orbital Transfer Vehicles*, Vol. 96, edited by H. F. Nelson, AIAA, 1985, pp. 3–53.

[16] Blottner, F., Johnson, M., and Ellis, M., "Chemically Reacting Gas Viscous Flow Program for Multi-Component Gas Mixtures," Tech. Rep. SC-RR–70-754, Sandia National Laboratories, 1971.

[17] Wilke, C., "A Viscosity Equation for Gas Mixtures," *The Journal of Chemical Physics*, Vol. 18, No. 4, 1950, pp. 517–519.

[18] Mortensen, C. H., and Zhong, X., "High-Order Shock-Fitting Method for Hypersonic Flow with Graphite Ablation and Boundary Layer Stability," *AIAA 2012-3150*, 2012.

[19] Mortensen, C. H., and Zhong, X., "Numerical Simulation of Graphite Ablation Induced Outgassing Effects on Hypersonic Boundary Layer Receptivity over a Cone Frustum," *AIAA 2013-0522*, 2013.

[20] Mortensen, C. H., and Zhong, X., "Real Gas and Surface Ablation Effects on Hypersonic Boundary Layer Instability over a Blunt Cone," *AIAA 2013-2981*, 2013.

[21] Mortensen, C. H., and Zhong, X., "Simulation of Second-Mode Instability in a Real-Gas Hypersonic Flow with Graphite Ablation," *AIAA Journal*, Vol. 52, No. 8, 2014, pp. 1632–1652.

[22] Mortensen, C. H., and Zhong, X., "Numerical Simulation of Hypersonic Boundary-Layer Instability in a Real Gas with Two-Dimensional Surface Roughness," *AIAA 2015-3077*, 2015.

[23] Mortensen, C. H., "Effects of Thermochemical Nonequilibrium on Hypersonic Boundary-Layer Instability in the Presence of Surface Ablation and Isolated Two-Dimensional Roughness," Ph.D. thesis, University of California Los Angeles, 2015.

[24] Pruett, D. C., and Chang, C.-L., "Spatial Direct Numerical Simulation of High-Speed Boundary-Layer Flows Part II: Transition on a Cone in Mach 8 Flow," *Theoretical and Computational Fluid Dynamics*, Vol. 7, 1995, pp. 397–424.

[25] Liu, Y., and Vinokur, M., "Nonequilibrium Flow Computations. I. An Analysis of Numerical Formulations of Conservation Laws," *Journal of Computational Physics*, Vol. 83, No. 2, 1989, pp. 373–397.

[26] Shu, C.-W., and Osher, S., "Efficient implementation of essentially non-oscillatory shock-capturing schemes," *Journal of Computational Physics*, Vol. 77, No. 2, 1988, pp. 439–471.

[27] Knisely, C., and Zhong, X., "An Investigation of Sound Radiation by Supersonic Unstable Modes in Hypersonic Boundary Layers," *AIAA 2017-4516*, 2017.

[28] Knisely, C., "Supersonic Unstable Modes in Hypersonic Boundary Layers with Thermochemical Nonequilibrium Effects," Ph.D. thesis, University of California, Los Angeles, 2018.

[29] Knisely, C., and Zhong, X., "Impact of Vibrational Nonequilibrium on the Supersonic Mode in Hypersonic Boundary Layers," *AIAA Journal*, Vol. 58, No. 4, 2019.

[30] Fedorov, A., and Tumin, A., "High-speed boundary-layer instability: old terminology and a new framework," *AIAA Journal*, Vol. 49, No. 8, 2011, pp. 1647–1657.

[31] Balakumar, P., "Receptivity of Supersonic Boundary Layers Due To Acoustic Disturbances Over Blunt Cones," *AIAA 2007-4491*, 2007.

[32] Gaydos, P., and Tumin, A., "Multimode Decomposition in Compressible Boundary Layers," *AIAA Journal*, Vol. 42, No. 6, 2004, pp. 1115–1121.

[33] Miselis, M., Huang, Y., and Zhong, X., "Modal Analysis of Receptivity Mechanisms for a Freestream Hot-Spot Perturbation on a Blunt Compression-Cone Boundary Layer," *AIAA 2016-3345*, 2016.

[34] Ma, Y., and Zhong, X., "Receptivity of a supersonic boundary layer over a flat plate. Part 1. Wave structures and interactions," *Journal of Fluid Mechanics*, Vol. 488, 2003, pp. 31–78.

[35] Varma, A., Knisely, C. P., and Zhong, X., "Three-Dimensional Receptivity of a Hypersonic Straight Cone Boundary Layer to a Freestream Vorticity Disturbance," *AIAA 2023-1042*, 2023.

[36] He, S., and Zhong, X., "The effects of nose bluntness on broadband disturbance receptivity in hypersonic flow," *Physics of Fluids*, Vol. 34, 2022.

[37] Marineau, E. C., Grossir, G., Wagner, A., Leinemann, M., Radespiel, R., Tanno, H., Chynoweth, B. C., Schneider, S. P., Wagnild, R. M., and Casper, K. M., "Analysis of Second-Mode Amplitudes on Sharp Cones in Hypersonic Wind Tunnels," *Journal of Spacecraft and Rockets*, Vol. 56, No. 2, 2019, pp. 307–318.